JTTEE5 19:156–167
DOI: 10.1007/s11666-009-9424-0
1059-9630/$19.00 © ASM International

Peer Reviewed

Degradation of Thermal Barrier Coatings by Fuel Impurities and CMAS: Thermochemical Interactions and Mitigation Approaches

Prabhakar Mohan, Travis Patterson, Bo Yao, and Yongho Sohn

(Submitted July 20, 2009; in revised form September 1, 2009)

Degradation of free-standing yttria-stabilized zirconia (YSZ) and CoNiCrAlY coatings (300 μm) due to V_2O_5 and a laboratory-synthesized CMAS was investigated at temperatures up to 1400 °C. Reactions, phase transformations, and microstructural development in coatings were examined by using x-ray diffraction, scanning electron microscopy, and transmission electron microscopy. The molten deposits destabilized the YSZ and reacted with the thermally grown oxide with various phase transformations and reaction product formation. A dense, continuous environmental barrier overlay, based on oxides, applied by electrophoretic deposition was effective in mitigating the molten deposit attack. Enriching CMAS composition with Al promoted the crystallization of anorthite platelets and $MgAl_2O_4$ spinel, and mitigated CMAS ingression. EPD MgO overlay was also effective in protection against V_2O_5 melt by formation of magnesium vanadates. EPD alumina overlay deposited on thermal barrier coatings with APS 8YSZ and bond-coated IN939 superalloy retained its adhesion and structural integrity after prolonged furnace thermal cycle test at 1100 °C.

Keywords air plasma spray, barrier overlay coatings, CMAS sand, environmental degradation, thermal barrier coatings, vanadium pentoxide

1. Introduction

Advanced gas turbine engines employ thermal barrier coatings (TBCs) to insulate hot-section metallic components. TBCs have become a critical technology for improving efficiency and performance of advanced gas turbines (Ref 1-4). TBCs are multilayered systems consisting of a ceramic topcoat, typically YSZ (ZrO_2 stabilized with 7-8 wt.% Y_2O_3) for thermal insulation, a thermally grown oxide (TGO) scale, a metallic bond coat that also provides oxidation/corrosion resistance, and a superalloy substrate. The YSZ coatings are generally deposited either by air plasma spray (APS) or electron beam physical vapor deposition (EB-PVD) techniques. TBCs possess their long-term durability at high temperatures with high strain compliance and the long-term thermal stability of the YSZ topcoat that is desirably composed of the metastable, tetragonal-prime ZrO_2 phase (t′-ZrO_2). The t′-ZrO_2 phase that is typically achieved due to rapid quench during the YSZ coating processing, helps prevent the disruptive phase transformation to equilibrium phases of monoclinic (m) and fluorite-cubic (f) ZrO_2 ($t' \rightarrow t + f \rightarrow m + f$) during thermal cycling. The TGO scale that forms between the YSZ topcoat and the metallic bond coat significantly influences the durability of TBCs (Ref 5). The bond coat is primarily designed as a local Al reservoir for facilitating the formation of α-Al_2O_3 as the protective TGO scale. MCrAlY (M = Ni and/or Co) bond coats are typically deposited by low-pressure plasma spraying. Developments in thermal spray processing techniques of MCrAlY type bond coats identified high velocity oxy-fuel, conventional air plasma spraying, vacuum plasma spraying, and high frequency pulse detonation as alternate cost-effective techniques (Ref 6).

When cost-effective alternative fuels that contain appreciable levels of elemental impurities such as V, Na, S, P, and Ca are used, corrosive compounds such as vanadates and sulfates might arise as combustion by-products (Ref 7, 8). In addition, TBCs are also increasingly susceptible to degradation by air-ingested CMAS deposits, especially in aircraft engines that operate in a dust-laden environment (Ref 9-12). These aggressive compounds can deposit, melt, and degrade the TBCs via repeated freeze-thaw action and, to a certain extent, direct chemical reaction with TBC constituents. The thermo-mechanical and thermo-chemical interactions can accelerate the failure of TBCs and underlying components by

This article is an invited paper selected from presentations at the 2009 International Thermal Spray Conference and has been expanded from the original presentation. It is simultaneously published in *Expanding Thermal Spray Performance to New Markets and Applications: Proceedings of the 2009 International Thermal Spray Conference*, Las Vegas, Nevada, USA, May 4-7, 2009, Basil R. Marple, Margaret M. Hyland, Yuk-Chiu Lau, Chang-Jiu Li, Rogerio S. Lima, and Ghislain Montavon, Ed., ASM International, Materials Park, OH, 2009.

Prabhakar Mohan, Travis Patterson, Bo Yao, and **Yongho Sohn**, Advanced Materials Processing and Analysis Center (AMPAC) and Department of Mechanical, Materials and Aerospace Engineering, University of Central Florida, Orlando, FL 32816. Contact e-mail: ysohn@mail.ucf.edu.

various deleterious mechanisms such as destabilization of the YSZ topcoat ($t' \rightarrow t+f \rightarrow m+f$), accelerated oxidation and hot corrosion of underlying metallic bond coat and superalloy substrate (Ref 7-17).

Infiltration of molten deposits into the porous YSZ topcoat has been frequently reported (Ref 8, 11), and warrants an understanding of the interaction of such corrosive molten deposits with the underlying metallic bond coat. Thus, resistance against melt-induced degradation is one of the critical durability issues for TBCs. In this study, detailed investigations are highlighted to understand the individual chemical interactions of APS 8YSZ and CoNiCrAlY coatings with deposits such as V_2O_5 and CMAS at elevated temperatures. To protect TBCs from both thermomechanical and thermochemical degradation of molten deposits, melt ingression into the porous YSZ topcoat must be suppressed. Promising approaches to mitigate the molten deposit attack of TBCs can be categorized into (i) employing an impermeable surface coating for TBCs that can act as an inert barrier (Ref 18), (ii) utilizing a sacrificial overlay that can trap deposit melt through chemical interactions, which could potentially result in increased melting temperature and viscosity of deposit melt (Ref 19)—a method examined in this study (Ref 20, 21), (iii) surface sealing of the YSZ topcoat (Ref 22), and (iv) modifying the ceramic topcoat chemistry (Ref 23-25). In this contribution, processing of a dense, continuous environmental barrier overlay, applied by electrophoretic deposition (EPD) is introduced. EPD is a versatile and ''scale-up-ready'' manufacturing technique that can produce crack-free overlay coatings of controlled thickness and porosity, uniform pore-distribution with improved microstructural homogeneity and superior adhesion (Ref 26-29).

2. Experimental Details

2.1 Free-Standing APS YSZ and CoNiCrAlY Coatings

Free-standing YSZ coatings were produced by depositing ZrO_2-8 wt.% Y_2O_3 (8YSZ) powders with an average particle size of 106 μm (Praxair Inc., Danbury, CT) on grit-blasted graphite substrates using Sulzer-Metco F4 MB plasma torch (Westbury, NY). Processing details include a spraying current of 675 A with a primary gas Ar flow of 100 SCFH (standard cubic feet per hour), a secondary gas H_2 flow of 20 SCFH, and a carrier gas Ar flow of 8 SCFH. Graphite substrates are later burnt off to obtain the free-standing YSZ coatings. Similarly, free-standing APS CoNiCrAlY coatings were produced by depositing CoNiCrAlY powders (CO-159, Praxair Inc., Danbury, CT) of composition 38.5 wt.% Co, 32 wt.% Ni, 21 wt.% Cr, 8 wt.% Al, and 0.5 wt.% Y, on graphite substrates that were later burnt off. A spraying current of 675 A with a primary gas Ar flow of 120 SCFH, a secondary gas H_2 flow of 18 SCFH, and a carrier gas Ar flow of 8 SCFH was employed. Both free-standing APS 8YSZ and CoNiCrAlY coating specimens were 300 μm in thickness for all experiments. The CoNiCrAlY coatings were oxidized at 1100 °C for 50 h to have coating microstructure with internal oxidation and appreciably thick TGO on surface that is likely to be exposed to molten deposits in a real engine operation.

2.2 Molten Deposit Testing at Elevated Temperature

To examine the individual thermochemical interactions of the APS YSZ and CoNiCrAlY coatings with V_2O_5 and CMAS at elevated temperatures, reactions with each compound were examined individually. Specimens in contact with V_2O_5 and a laboratory-synthesized CMAS were subjected to isothermal heat-treatment at temperature ranging from 700 to 1400 °C for durations up to 5 h in air. The contaminants in the form of powder were spread uniformly with a concentration of 10 mg/cm^2 in case of V_2O_5 and 20 mg/cm^2 for CMAS. The concentrations of contaminants were chosen to examine the mechanisms of degradation at an accelerated rate. Based on the average composition of CMAS deposits reported (Ref 20), CMAS was synthesized with a chemical composition of 33CaO-9MgO-13$AlO_{1.5}$-45SiO_2 (mole %) by mechanical milling (SPEX CretPrep, Metuchen, NJ) for 1 h at room temperature.

2.3 Microstructural Characterization

X-ray diffraction studies were performed on tested specimens to examine the development of constituent phases by using a Rigaku D-Max B Diffractometer (Tokyo, Japan) with Cu K_α radiation. Morphological and cross-sectional microstructural analyses were carried out to examine the melt interactions using a JEOL 6400F field-emission scanning electron microscope (FE-SEM) (Tokyo, Japan) equipped with x-ray energy dispersive spectrometer (XEDS) A Philips/FEI Tecnai F30 300 keV transmission electron microscope (TEM) (Hillsboro, OR, USA), equipped with high angle annular dark field (HAADF), and XEDS was also employed for a detailed examination of the phase constituents of coating specimens after thermochemical interaction with molten deposits. The sample preparation for TEM was performed by focused ion beam (FIB) in-situ lift-out (INLO) using a FEI 200 TEM FIB (Hillsboro, OR, USA).

2.4 Environmental Barrier Overlay Coatings for TBCs by EPD

We attempted to fabricate dense overlay coatings of Al_2O_3 and MgO to protect TBCs against CMAS and V_2O_5, respectively, by EPD followed by a sintering step. To achieve dense overlay coatings of Al_2O_3 and MgO on the YSZ, stable colloidal suspensions of Al_2O_3 (0.3 μm α-Al_2O_3 powder, Metlab Corporation, Niagara Falls, NY) and MgO powders (1 μm, Mallinckrodt Baker, Inc., Phillipsburg, NJ) were individually prepared by dispersing appropriate powders in an acetone-ethanol (Fisher Scientific, Pittsburgh, PA) organic solvent mixture (volume ratio 1:1) with a solid loading of 10 g/L with a dispersant

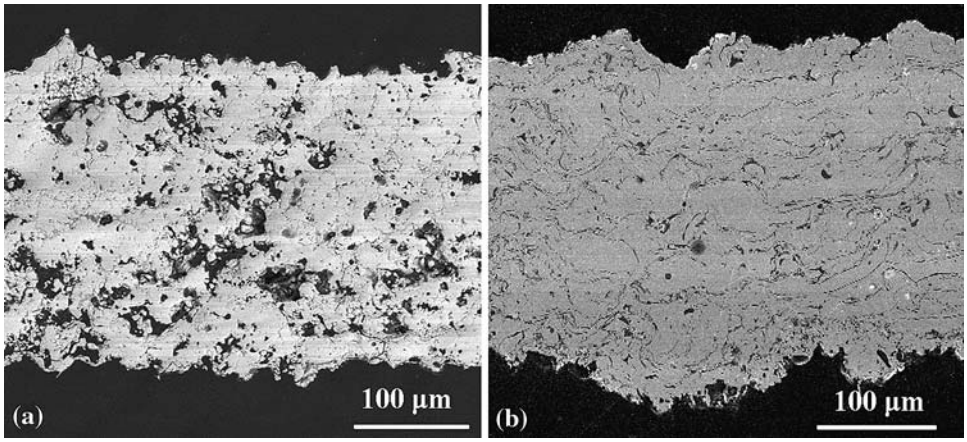

Fig. 1 Cross-sectional microstructures of as-sprayed free-standing (a) YSZ topcoat and (b) CoNiCrAlY bond coat (Ref 8, 17)

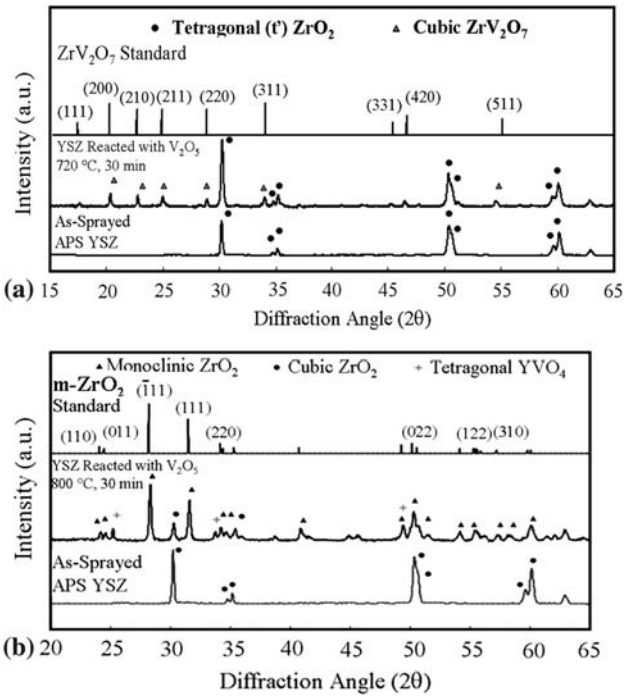

Fig. 2 XRD patterns obtained from the YSZ interacted with V_2O_5 melt for 2 h: (a) at 720 °C with the reaction product ZrV_2O_7 and (b) at 800 °C with the ZrO_2 phase transformation and YVO_4 formation (Ref 8)

additive of iodine at a concentration of 0.4 g/L. High proton concentration that yields a strong positive charge to the dispersed oxide powders was evident from a measured pH value of 0.6 for such colloidal dispersion. Electrically conductive APS YSZ (Au-Pd sputter coated) that was made cathode, and an inert graphite anode were completely immersed in the colloidal suspension that was constantly stirred. A DC voltage of 30 V was applied between the cathode and anode using a Protek 3032B DC power supply. During EPD, positively charged particles (Al_2O_3 or MgO) were drifted, and deposited on the APS YSZ cathode for durations ranging up to 15 min.

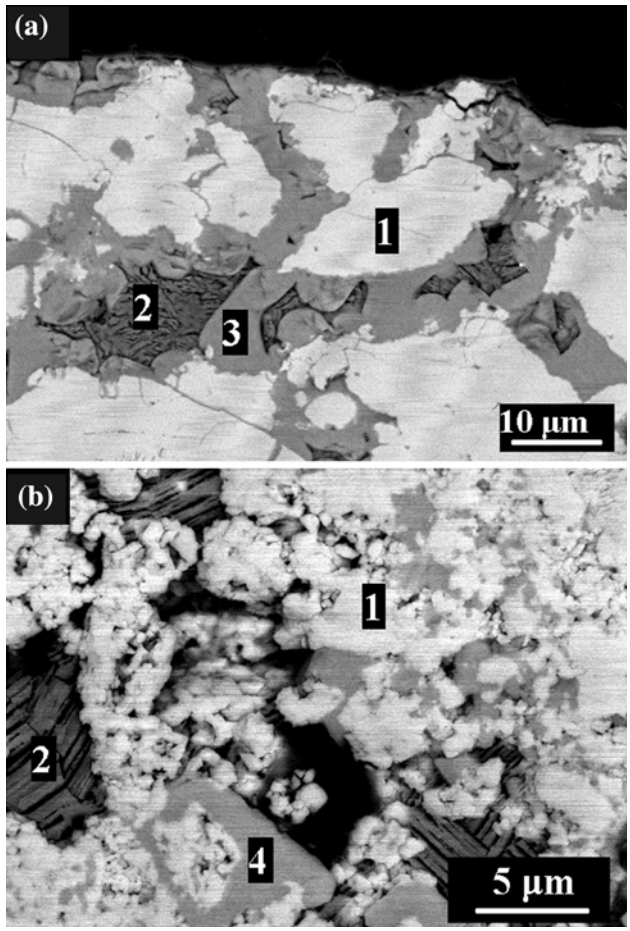

Fig. 3 Cross-sectional backscattered electron micrographs of the YSZ reacted with V_2O_5 (a) at 720 °C that reveal unaffected YSZ (region 1) and ZrV_2O_7 (region 3) reaction product, and (b) at 800 °C showing the reaction product YVO_4 (region 4) along with solidified V_2O_5 residual (region 2) (Ref 8)

The EPD powder compact was dried in ambient atmosphere for 2 h and subjected to densification by sintering. Sintering was performed at 1200 °C for Al_2O_3 and

1100 °C for MgO for 10 h with a carefully controlled ramp up and ramp down rates of 2 °C/min. After sintering, free-standing modified-YSZ consisting of 300 μm thick APS YSZ with a uniform crack-free dense EPD overlay was obtained. While the temperature of densification by sintering employed in this study is too high for bond-coated superalloys, use of smaller powders can reduce the time and temperature of this sintering processing. Modified free-standing topcoat assembly was also subjected to high temperature molten deposit exposure testing, and relevant microstructural investigation was performed in detail by XRD, SEM, XEDS, and TEM. With due consideration for real applications, durability of EPD alumina overlay on a 8YSZ/CoNiCrAlY/IN939 TBC specimen was also examined by furnace thermal cyclic test using CM 1710 Rapid High Temperature Furnace. A 30-μm thick EPD alumina overlay was deposited on top of the APS YSZ applied on bond-coated IN939. For furnace thermal cycling in air, each thermal cycle consisted of 10 min heat up to 1100 °C, 60 min hold at 1100 °C, followed by 10 min forced air quench. Adhesion and structural integrity of the EPD alumina overlay were examined after 20 thermal cycles by cross-sectional microstructural analysis.

3. Results

3.1 Free-Standing YSZ and CoNiCrAlY Coatings

As-sprayed free-standing 8YSZ and CoNiCrAlY coatings produced by APS were characterized for initial phase constituents and microstructure. The YSZ was found to primarily consist of t′-ZrO_2, which is the desirable phase for TBC applications. Initial microstructure of free-standing APS YSZ coating of 300 μm thickness is presented in Fig. 1(a). Characteristic splat-quenched microstructure of typical APS YSZ coatings, such as inter-splat boundary and microcracks were clearly seen. Secondary electron micrograph exhibiting the cross-sectional morphology of APS CoNiCrAlY coating is illustrated in Fig. 1(b).

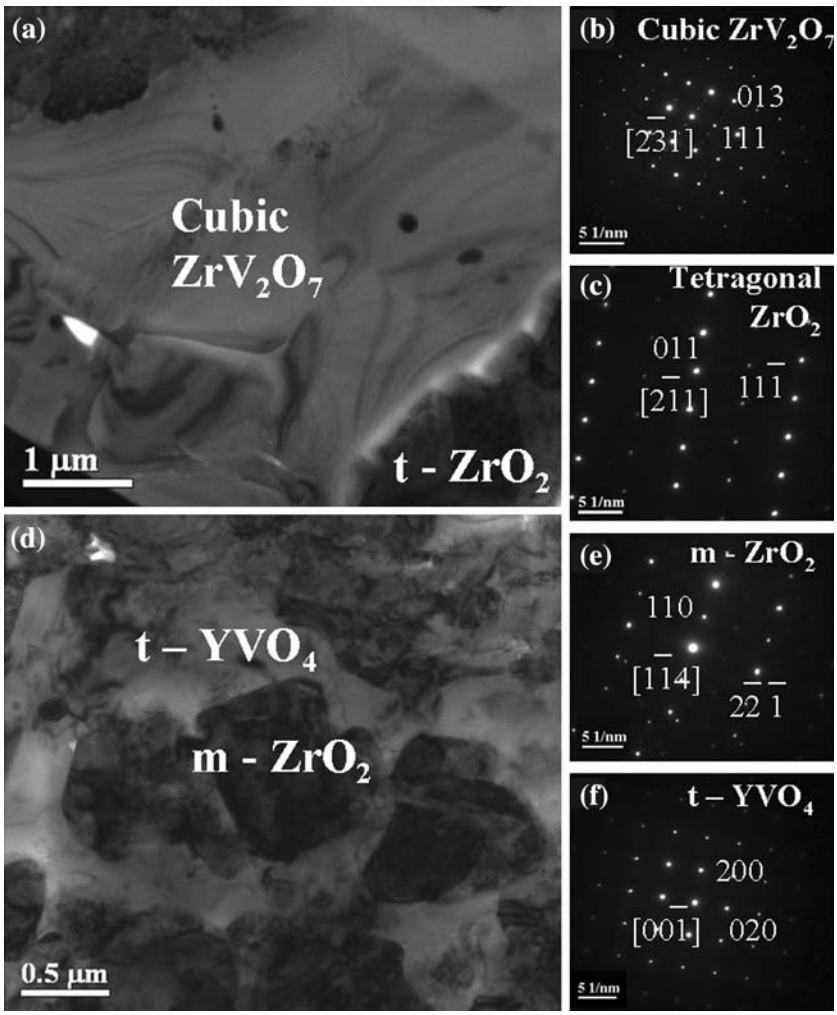

Fig. 4 Bright field TEM micrographs (a and d) and selected area electron diffraction patterns (b, c, e, and f) obtained from the YSZ reaction with V_2O_5 melt. The phase constituents of the YSZ after the reaction at 720 °C are cubic ZrV_2O_7 and tetragonal ZrO_2, and the phase constituents of the YSZ after reaction at 800 °C are tetragonal YVO_4 and monoclinic ZrO_2 (Ref 8)

3.2 Degradation of Free-Standing YSZ and CoNiCrAlY Coatings by V_2O_5 Melt

Degradation of APS YSZ and CoNiCrAlY coatings by V_2O_5 melt were individually studied at elevated temperatures ranging from 700 to 900 °C (Ref 8, 17). Figure 2(a) and (b) shows the XRD patterns obtained from the YSZ reacted with V_2O_5 at 720 and 800 °C for 30 min, respectively. At 720 °C, ZrV_2O_7 was identified as the only reaction product with no evidence of monoclinic (m) ZrO_2 formation. However at 800 °C, a complete phase transformation of t′-ZrO_2 to monoclinic (m) and fluorite-cubic (f) ZrO_2 phases was observed due to the reaction of V_2O_5 with Y_2O_3 stabilizer that produced yttrium vanadate, YVO_4. Microstructural analysis as demonstrated by cross-sectional backscattered electron micrographs presented in Fig. 3 reveals a significant infiltration of V_2O_5 into porous YSZ, which results in the formation of ZrV_2O_7 at 720 °C and YVO_4 at 800 °C. Detailed microstructural and electron diffraction studies performed by TEM revealed the presence of cubic ZrV_2O_7 and tetragonal ZrO_2 after reaction at 720 °C as shown in Fig. 4. Formation of tetragonal YVO_4 at 800 °C that resulted in disruptive ZrO_2 phase transformation (t′ → t + f → m + f) was also confirmed as presented in Fig. 4.

Interactions of V_2O_5 melt with preoxidized CoNiCrAlY coatings were examined at 700 and 900 °C for 2 h (Ref 17). XRD patterns in Fig. 5(a) revealed the formation of (Cr, Al)VO_4 at 700 °C with minimal interactions evidenced by the presence of unreacted V_2O_5 melt. At 900 °C, a complete consumption of V_2O_5 melt by CoNiCrAlY with the formation of (Co, Ni)$_3(VO_4)_2$ and (Ni, Co)(Cr, Al)$_2O_4$ as presented by XRD in Fig. 5(b). The surface morphology and cross-sectional microstructure of APS CoNiCrAlY after interaction with V_2O_5 are presented by secondary electron and backscattered electron micrographs in Fig. 6. Based on the Al/Cr ratio determined by XEDS, the reaction product of (Cr, Al)VO_4 at 700 °C was found to have two different morphologies: thin large platelets of 5 μm in diameter (Al-rich region 1 in Fig. 6a) and uniformly fine grains of 1 μm in size (Cr-rich region 2 in Fig. 6a). Figure 6(b) reveals the crystals of cobalt-nickel orthovanadate (region 3) formed at 900 °C with variation in size up to 15 μm. Unlike the limited interaction observed at 700 °C, extensive degradation via dissolution of CoNiCrAlY by V_2O_5 melt with the formation of (Co, Ni)$_3(VO_4)_2$ and (Ni, Co)(Cr, Al)$_2O_4$ was observed at 900 °C as presented in Fig. 6(c). An interaction layer greater than 150 μm in thickness was observed due to accelerated oxidation accompanied by oxide dissolution by V_2O_5 melt, resulting in various reaction products.

3.3 Degradation of Free-Standing YSZ and CoNiCrAlY Coatings by CMAS Melt

The interaction between the YSZ and CMAS was observed to occur only for elevated temperatures starting at 1250 °C, where CMAS was found to completely melt and infiltrate the YSZ coatings (Ref 11). XRD patterns

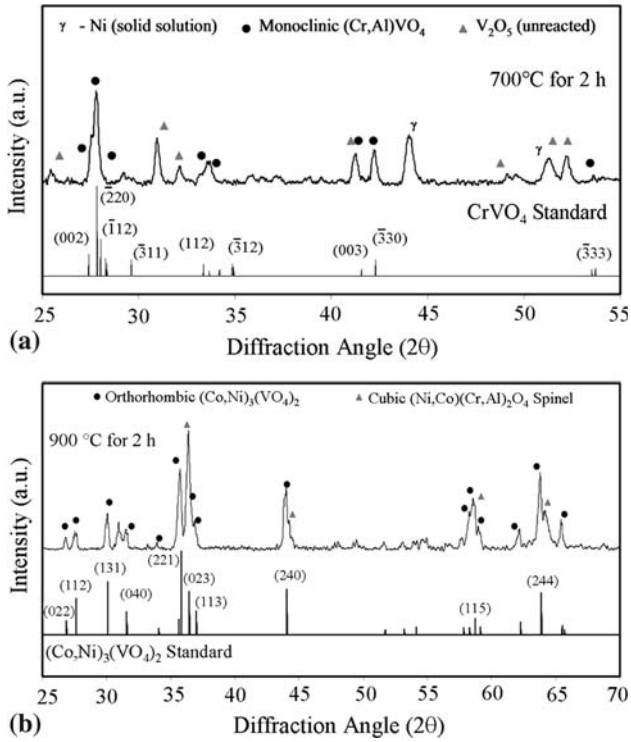

Fig. 5 XRD patterns obtained from free-standing CoNiCrAlY coatings exposed to V_2O_5 melt at (a) 700 °C and (b) 900 °C for 2 h revealing the different reaction mechanisms (Ref 17)

obtained from the YSZ infiltrated by CMAS at 1300 °C for 4 h are presented in Fig. 7. The disruptive phase transformation of t′-ZrO_2 to (m + f) ZrO_2 (i.e., t′ → t + f → m + f) has clearly occurred. The transition of the two adjacent Bragg reflections from (103) and (211) of tetragonal phase to one single peak that corresponds to the reflection from (311) cubic phase is evident in the magnified view of shaded region as shown in Fig. 7. Similar XRD patterns were obtained for all specimens when CMAS infiltration had occurred. This phase transformation to Y_2O_3-depleted monoclinic ZrO_2 and Y_2O_3-rich cubic ZrO_2 phases is attributed to a deviation in the Y_2O_3 content from the 8YSZ solid solution during degradation by CMAS (Ref 11). Cross-sectional backscattered electron micrographs of the YSZ infiltrated by molten CMAS at 1300 °C for 4 h are shown in Fig. 8. Cross-sectional microstructural analysis revealed a similar microstructure for all samples that suffered CMAS attack at temperature above 1250 °C. Infiltration of CMAS melt through the interconnected pores and cracks of the YSZ resulted in a dissolution of the YSZ, followed by the reprecipitation of ZrO_2 grains with a different microstructure and composition based on the local melt chemistry. The reprecipitation of spherical ZrO_2 grains is clearly seen in Fig. 8(b). Bright field TEM micrographs obtained from the YSZ specimen subjected to molten CMAS degradation at 1350 °C for 2 h revealed the presence of various phases as shown in Fig. 9. Similar to XRD results, both t′-ZrO_2 and m-ZrO_2 were present in

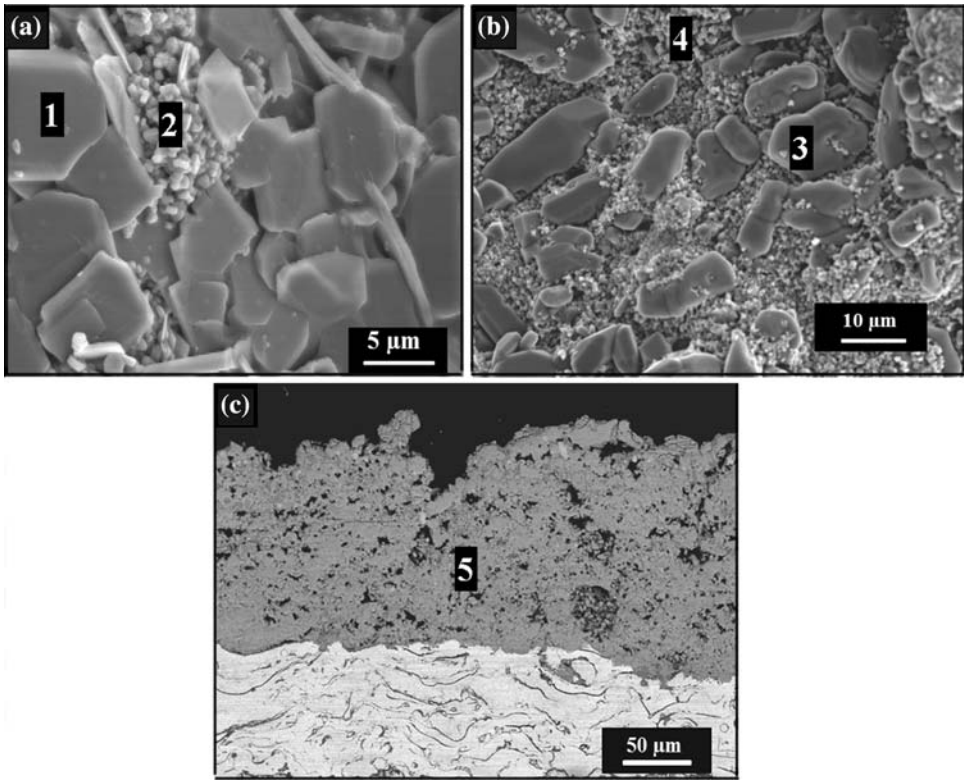

Fig. 6 Secondary electron micrographs from free-standing CoNiCrAlY coatings showing the surface morphology of various reaction products obtained at (a) 700 °C and (b) 900 °C for 2 h: Regions 1 and 2 correspond to (Cr, Al)VO_4 with different Al/Cr ratio; Region 3 corresponds to (Co, Ni)$_3$(VO_4)$_2$; Region 4 corresponds to (Ni, Co)(Cr, Al)$_2O_4$. (c) Cross-sectional backscattered electron micrograph showing the thick reaction scale (region 5) due to V_2O_5 reaction at 900 °C for 2 h (Ref 17)

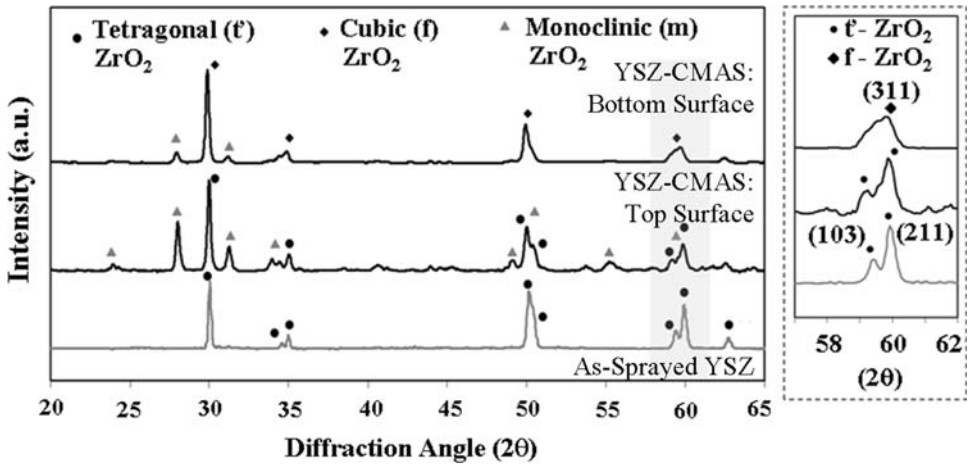

Fig. 7 XRD patterns obtained from the free-standing YSZ after infiltration/reaction by CMAS at 1300 °C for 4 h confirming the presence of various phase constituents at top and bottom surfaces of the YSZ (Ref 11)

the CMAS infiltrated specimens. The electron diffraction patterns obtained from the three primary regions were indexed as t′-ZrO_2, m-ZrO_2 and completely amorphous CMAS glass. Few localized spots in amorphous CMAS were identified to be extremely richer in Y content compared to Zr content by XEDS.

Preoxidized APS CoNiCrAlY coatings were exposed to CMAS melt at 1250 °C for 5 h. Secondary electron micrographs obtained after interaction with CMAS revealed the crystallization of applied CMAS as seen in Fig. 10(a). CMAS crystallization consumed the TGO, α-Al_2O_3, and formed spinel oxide, (Ni, Co)(Al,Cr)$_2O_4$.

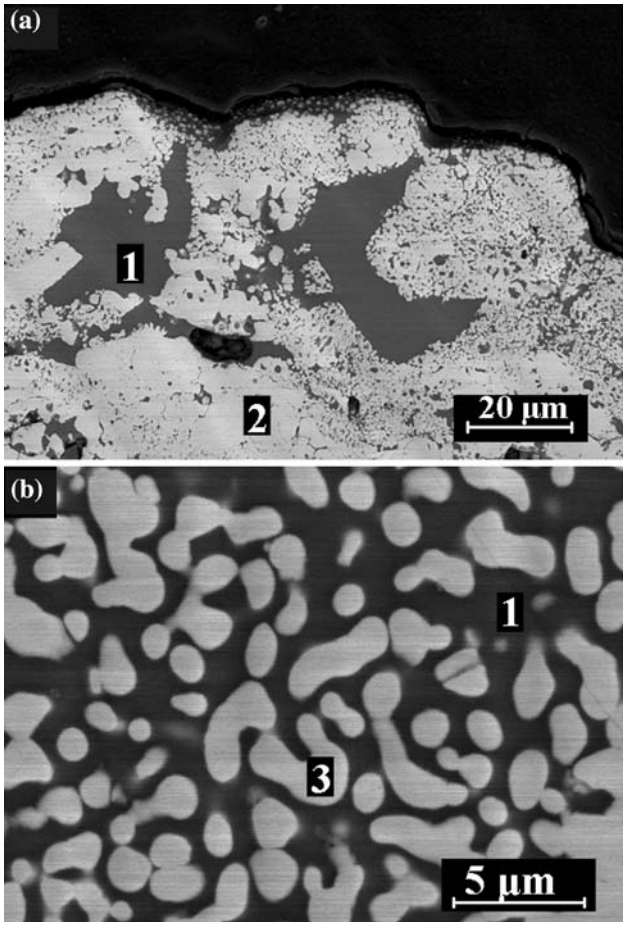

Fig. 8 Backscattered electron micrographs obtained from the YSZ after interaction with CMAS melt at 1300 °C for 4 h that show the CMAS melt ingression and spherical reprecipitated ZrO_2 grains. (a, b) Regions 1, 2, and 3 correspond to CMAS island, unaffected YSZ, and reprecipitated ZrO_2 grains, respectively (Ref 11)

Reaction products as thin platelets are visible in the cross-sectional backscattered electron micrograph as shown in Fig. 10(b). From EDS analysis, these platelets were found to be rich in Al content compared to that of applied CMAS, which confirmed the dissolution of the TGO, α-Al_2O_3. Crystallization of CMAS glass through enrichment of Al content has been reported earlier (Ref 23), where Anorthite, $CaAl_2Si_2O_8$ were found to be the predominant crystallites. Hence, α-Al_2O_3 that promotes the crystallization of CMAS, has been studied in this study as an environmental barrier overlay for TBCs.

3.4 EPD Barrier Overlay Coatings for TBCs

3.4.1 EPD Al_2O_3 Overlay Coatings and Suppression of CMAS Ingression. Crack-free Al_2O_3 overlay coatings were achieved through EPD using the aforementioned process parameters. Cross-sectional backscattered electron micrograph in Fig. 11(a) shows a continuous crack-free uniform Al_2O_3 overlay. Initial assessment of Al_2O_3 overlay microstructure reveals an excellent packing homogeneity associated with well-dispersed EPD suspension. The relative density was estimated to be approximately 95% through an image analysis. Secondary electron micrograph (Fig. 11b) showing the cross-sectional microstructure of Al_2O_3 overlay clearly illustrates the sintered microstructure evident from grain necking. Dense Al_2O_3 overlay coatings with such physical characteristics are promising in mitigating CMAS melt ingression, both physically (i.e., infiltration) and chemically (i.e., reaction). Interactions of EPD Al_2O_3 overlay with the CMAS melt, after exposure at 1300 °C for 1 h, are presented in Fig. 12. Secondary electron micrograph in Fig. 12(a) shows the crystallization of CMAS melt into platelets due to the thermochemical interactions with dense Al_2O_3 overlay. Complete suppression of CMAS melt ingression is clearly demonstrated in the cross-sectional backscattered electron micrograph presented in Fig. 12(b). The phase constituents of the as-processed EPD Al_2O_3 overlay and CMAS interacted alumina were examined by XRD and electron diffraction by TEM. Figure 13 presents the bright field TEM micrographs and electron diffraction patterns that highlight the predominant presence of anorthite $CaAl_2Si_2O_8$ platelets and equiaxed $MgAl_2O_4$ spinel (Ref 21). Crystallization of CMAS melt via thermochemical interaction with EPD Al_2O_3 overlay completely suppressed the ingression of CMAS into the YSZ coating.

3.4.2 EPD MgO Overlay Coating and Suppression of V_2O_5 Ingression. MgO has been commonly used as an injectant in gas turbines to chemically trap corrosive compounds such as sulfates and vanadates that arise from low-quality fuel. Figure 14(a) and (b) shows the crack-free and 25 μm-thick EPD MgO overlay on the YSZ coating. This coating assembly (free-standing APS YSZ with EPD MgO overlay) when subjected to V_2O_5 deposit at 800 °C for 1 h, was effective in suppressing the V_2O_5 melt ingression through chemical interactions. Formation of magnesium vanadates ($Mg_3V_2O_8$: $T_m = 1070$ °C and $Mg_2V_2O_7$: $T_m = 930$ °C) that have high melting temperatures compared to that of V_2O_5 melt (T_m: 690 °C) were identified as reaction products. Surface morphology of MgO reacted with molten V_2O_5 and the cross-sectional microstructure of interaction layer are illustrated in Fig. 14(c) and (d), respectively.

3.4.3 Thermal Cyclic Durability of EPD Overlay on TBC. We find that a dense overlay produced by EPD, which can be easily integrated into scale-up manufacturing, is effective in mitigating the molten deposit attack, particularly for the current commercial-production TBCs with APS and EB-PVD YSZ topcoats. However, the thermal expansion mismatch between the EPD overlay and the YSZ topcoat, and the possible deterioration of adhesion and structural integrity during service must be considered. The APS YSZ on APS CoNiCrAlY bond-coated IN939 superalloy specimen was modified with a 30-μm thick EPD Al_2O_3 overlay. After 20 1-h furnace thermal cycling at 1100 °C, we observed intact EPD Al_2O_3 overlay on top of the APS TBCs (Ref 21) as shown in Fig. 15.

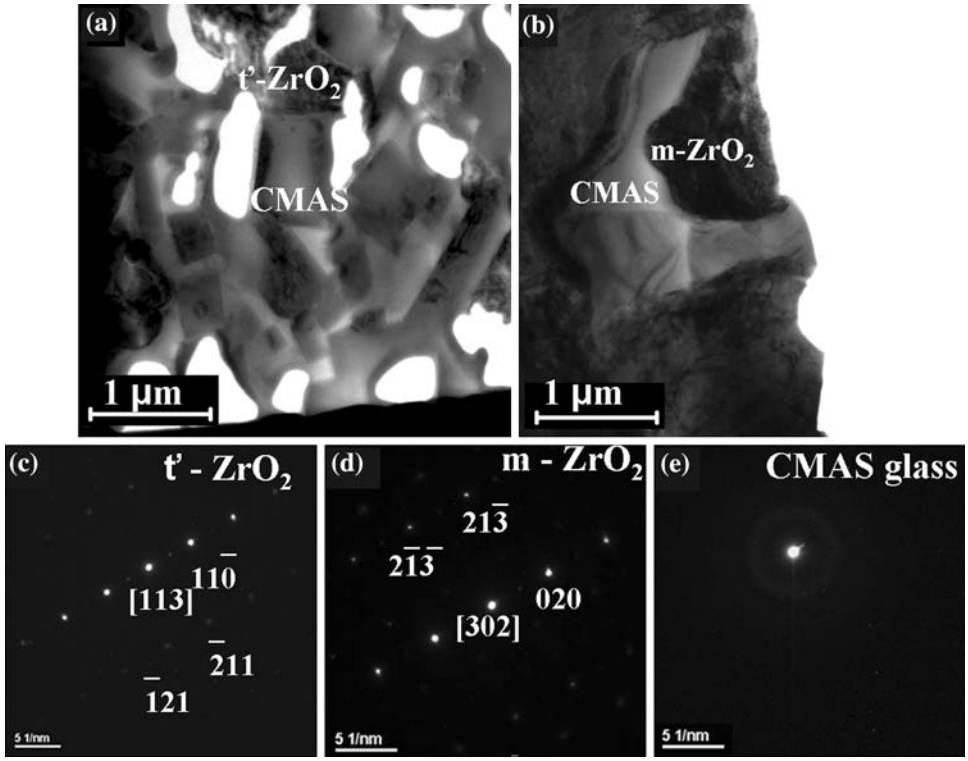

Fig. 9 (a,b) Bright field TEM micrographs of the YSZ after interaction with CMAS melt at 1350 °C for 2 h, and (c-e) relevant selected area electron diffraction patterns from tetragonal ZrO_2, monoclinic ZrO_2 and amorphous CMAS, respectively (Ref 11)

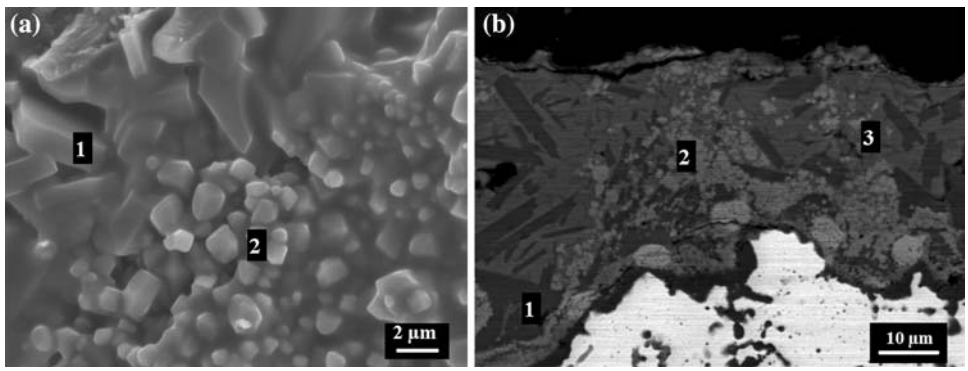

Fig. 10 (a) Secondary electron micrograph obtained from surface of CoNiCrAlY coating exposed to CMAS melt at 1250 °C for 5 h revealing the crystallization of CMAS (region 1) and spinel oxide formation (region 2). (b) Cross-sectional backscattered electron micrograph showing that the interaction layer composed of reaction product (region 1), spinel oxide (region 2), and unreacted CMAS (region 3)

4. Discussion

For all experimental temperature below 747 °C, YSZ was found to react with molten V_2O_5 through the formation of ZrV_2O_7. At temperature above 747 °C, V_2O_5 reacted with Y_2O_3 stabilizer to form YVO_4, and led to a disruptive ZrO_2 phase transformation ($t' \rightarrow t \rightarrow m + f$). YVO_4 is highly stable up to 1810 °C and acts as a low activity sink (i.e., leaching of the Y_2O_3 stabilizer) (Ref 8). The two different reactions observed could be explained based on the thermal instability of the reaction product, ZrV_2O_7. ZrV_2O_7 melts incongruently at 747 °C to ZrO_2 and a liquid with composition of 64% V_2O_5 + 36% ZrO_2 (Ref 8). This incongruent melting gave rise to the different reactions observed at 800 and 720 °C (i.e., above and below the incongruent melting temperature, respectively). At temperature above 747 °C, both liquid V_2O_5 from the incongruent melting of ZrV_2O_7 and unreacted V_2O_5 react

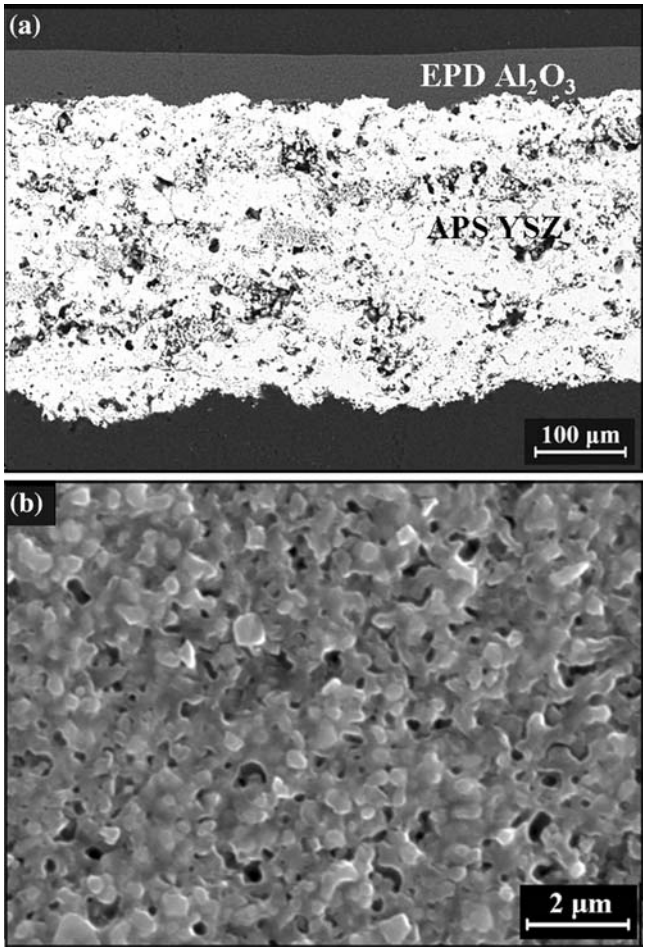

Fig. 11 Microstructure of EPD Al_2O_3 overlay on APS YSZ followed by sintering at 1200 °C for 10 h: (a) cross-sectional backscattered electron micrograph showing the continuous crack-free Al_2O_3 overlay on APS YSZ; (b) secondary electron micrograph revealing the surface morphology of Al_2O_3 overlay (Ref 21)

with Y_2O_3 to form YVO_4. In addition, pure solid ZrO_2 from the incongruent melting of ZrV_2O_7 would result in the formation of monoclinic phase. Reactions 1 and 2 given below represent the reaction mechanisms between the YSZ and V_2O_5 at temperatures below and above 747 °C, respectively.

$$ZrO_{2(s)}(\text{in YSZ}) + V_2O_{5(l)} \rightarrow ZrV_2O_{7(s)} + ZrO_{2(s)} \quad (t' \text{ in YSZ}) \quad \{\text{for } T < 747\,^{\circ}\text{C}\} \qquad \text{(Eq 1)}$$

$$Y_2O_{3(s)}(\text{in YSZ}) + V_2O_{5(l)} \rightarrow 2YVO_{4(s)} + \text{m-}ZrO_{2(s)} \quad \{\text{for } T > 747\,^{\circ}\text{C}\} \qquad \text{(Eq 2)}$$

Aforementioned, the V_2O_5 in reaction 2 could come from both incongruent melting of ZrV_2O_7 and the remaining V_2O_5.

APS CoNiCrAlY coatings degraded by V_2O_5 melt through two different mechanisms at 700 and 900 °C. V_2O_5 is a strong acidic oxide, and acidic dissolution of protective oxides such as Cr_2O_3 and Al_2O_3 readily occurred based on Lewis acid-base oxide reactions, where oxides of acidic and basic nature interact readily (Ref 5). At 700 °C, V_2O_5 melt was found to react with trivalent protective oxides to form (Cr, Al)VO_4. At elevated temperatures, these metal orthovanadates with lower melting temperatures (T_m: $AlVO_4$ = 695 °C, $CrVO_4$ = 810 °C) melt and promote further reaction. At 700 °C, the interaction was found to be minimal. However, at 900 °C, a significant consumption of coating constituents by V_2O_5 melt was evident, where the reaction product was observed to be (Ni, Co)$_3$(VO$_4$)$_2$. Metal orthovanadates of Ni and/or Co are stable up to 1300 °C (Ref 17). Dissolution rate of CoNiCrAlY by V_2O_5 melt was greater than the infiltration rate, and no residual V_2O_5 melt was observed. The V_2O_5 melt extensively consumed the CoNiCrAlY by forming a reaction scale 150 μm in thickness at 900 °C after 2 h. This region was found to have reaction products such as (Co, Ni)$_3$(VO$_4$)$_2$, YVO_4, and (Ni, Co)(Al,Cr)$_2$O$_4$. Thus the

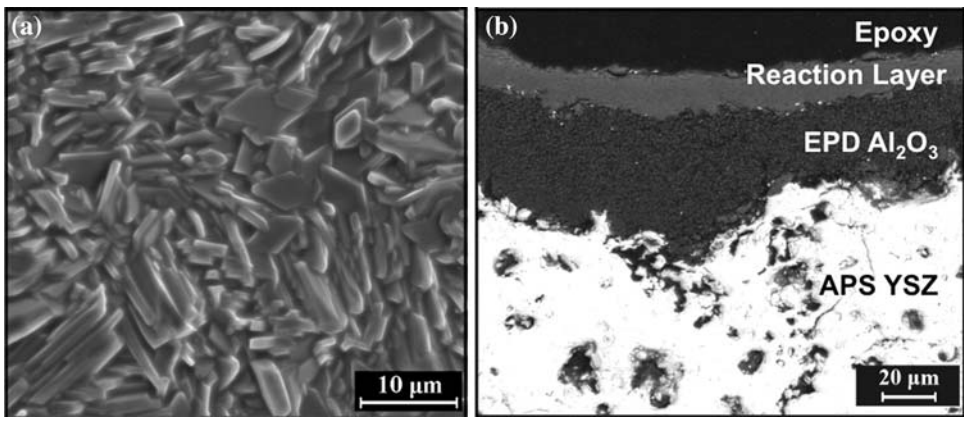

Fig. 12 Microstructural changes of EPD alumina overlay after interaction with CMAS melt at 1300 °C for 1 h: (a) secondary electron micrograph shows the formation of platelet crystals from CMAS and (b) cross-sectional backscattered electron micrograph demonstrating the complete suppression of CMAS melt ingression (Ref 21)

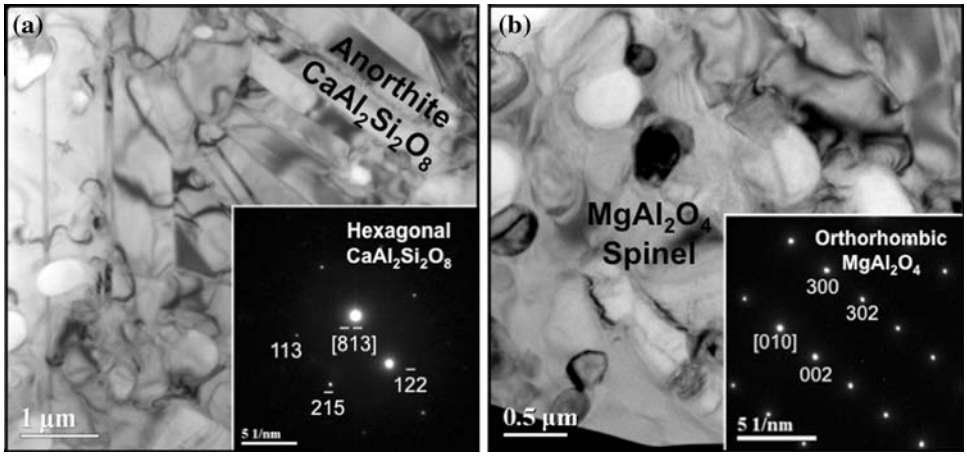

Fig. 13 Bright field TEM micrographs obtained from crystallized CMAS region highlighting the presence of (a) anorthite ($CaAl_2Si_2O_8$) platelets and (b) $MgAl_2O_4$ spinel with corresponding selected area electron diffraction patterns (Ref 21)

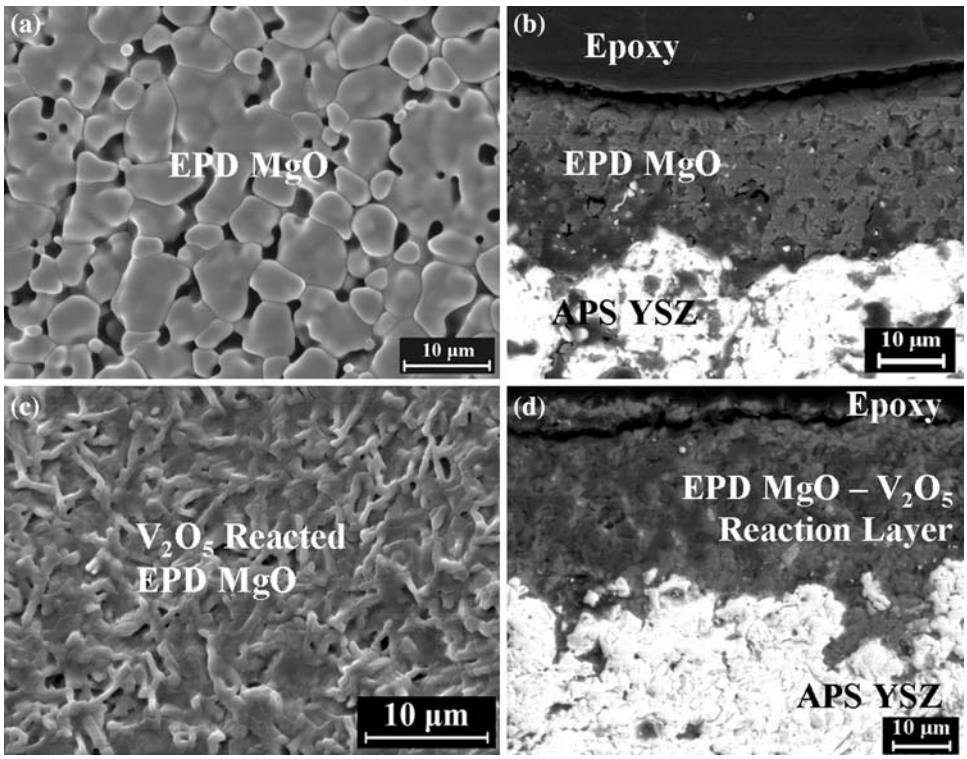

Fig. 14 Microstructural evolution of EPD MgO overlay for APS YSZ after interaction with V_2O_5 melt at 800 °C for 1 h: (a) and (c) secondary electron micrographs revealing the surface morphology of as-processed EPD MgO and V_2O_5 interacted MgO, respectively, showing morphological changes due to chemical interaction; (b) and (d) cross-sectional backscattered electron micrographs of as-processed MgO overlay on the YSZ and V_2O_5 interacted MgO overlay on APS YSZ, respectively (Ref 20)

V_2O_5-CoNiCrAlY interaction could be explained by the following reactions:

$$(Al_2O_3, Cr_2O_3)_{(s)} + V_2O_{5(l)} \rightarrow 2(Cr, Al)VO_{4(s)} \quad \{\text{for } T = 700\ ^\circ\text{C}\} \qquad \text{(Eq 3)}$$

$$3(NiO, CoO)_{(s)} + V_2O_{5(l)} \rightarrow (Co, Ni)_3(VO_4)_{2(s)} \quad \{\text{for } T = 900\ ^\circ\text{C}\} \qquad \text{(Eq 4)}$$

Interaction between the YSZ and CMAS was observed to occur starting at 1250 °C, where CMAS was found to melt and infiltrate the porous YSZ coating. CMAS melt in the YSZ resulted in dissolution of the YSZ followed by the reprecipitation of ZrO_2 grains with a different polymorphs and composition based on the local melt chemistry. The disruptive phase transformation of $t' \rightarrow t + f \rightarrow m + f$ occurred. This phase transformation to Y_2O_3-poor monoclinic ZrO_2 (m) and Y_2O_3-rich cubic ZrO_2 (f) phases

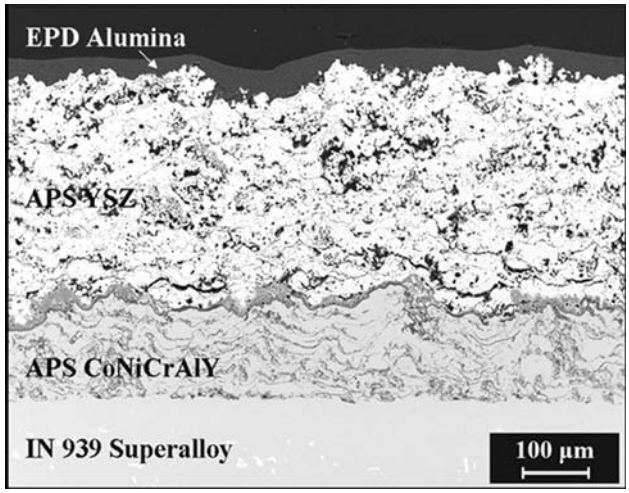

Fig. 15 Cross-sectional backscattered electron micrograph of a modified TBC (EPD Al_2O_3/APS YSZ/APS CoNiCrAlY) on IN939 superalloy after 1-h furnace thermal cyclic test at 1100 °C revealing the intact EPD Al_2O_3 overlay after 20 cycles (Ref 21)

is attributed to the deviation in the content of Y_2O_3 stabilizer from the original YSZ solid solution during reprecipitation (Ref 11). Top surface of the YSZ exposed to the CMAS melt was found to undergo the disruptive phase transformation to m-ZrO_2 significantly, whereas the bottom surface of the YSZ consisted primarily of cubic (f) ZrO_2. This could be due to an increase in Y content in CMAS during simultaneous dissolution of YSZ and ingression of CMAS melt through the thickness of the free-standing YSZ coating. Thus, reprecipitation of Y_2O_3-depleted monoclinic ZrO_2 at the top surface of the YSZ coating consequently increased the Y content in the CMAS melt and forced the reprecipitation of Y_2O_3-rich cubic ZrO_2 phase near the bottom surface of the YSZ. Preoxidized APS CoNiCrAlY coatings, when exposed to CMAS melt at 1250 °C for 5 h suffered dissolution of coating constituents that resulted in crystallization of applied CMAS into Al-rich phases, which were identified as Anorthite ($CaAl_2Si_2O_8$) and spinel (Ni, Co)(Al, $Cr)_2O_4$. An increase in Al content of CMAS shifts the CMAS glass composition to a easier-to-crystallize composition that produces anorthite has been reported earlier (Ref 23).

Dense Al_2O_3 overlay, successfully produced by EPD was found to be effective in mitigating CMAS attack. Due to the absence of interconnected pores/cracks in dense Al_2O_3 overlay, direct thermochemical interaction via dissolution of Al_2O_3 by CMAS melt was found to dominate over the CMAS infiltration. Crystallization of CMAS to anorthite (T_m: 1553 °C) and $MgAl_2O_4$ spinel (T_m: 2135 °C) completely arrested the CMAS melt ingression. Based on available CaO-SiO_2-Al_2O_3 ternary phase diagram, typical CMAS glass composition without considering the Mg content falls in pseudo-wollastonite field, whose glass composition is difficult to crystallize (Ref 23). Enrichment of Al content in CMAS shifts this ''difficult-to-crystallize'' pseudo-wollastonite glass composition to a ''crystallizable'' Al-rich glass composition that falls in the anorthite field. Thus the dissolution of α-Al_2O_3 by CMAS resulted in crystallization of CMAS to anorthite ($CaAl_2Si_2O_8$) platelets. Concurrently, the localized enrichment of Mg promoted the formation of $MgAl_2O_4$ spinel. Similarly, dense MgO overlay produced by EPD demonstrated the promising protection against corrosive V_2O_5 melt ingression. The 25-μm thick MgO overlay was found to be sufficient to completely suppress V_2O_5 melting ingression. Reactions to form magnesium vanadates ($Mg_3V_2O_8$ and $Mg_2V_2O_7$) that have higher melting temperature than the V_2O_5 melt would be beneficial to mitigate the V_2O_5 and similar acidic oxide attack on TBCs by increasing the melting temperature and viscosity of such molten deposits. Observation made from 1-h furnace thermal cyclic test at 1100 °C for EPD Al_2O_3 overlay on TBC system (i.e., APS YSZ/CoNiCrAlY bond coat/IN939 superalloy) demonstrated the thermal cyclic durability of EPD overlay (Ref 21).

5. Summary

Free-standing APS YSZ and CoNiCrAlY coatings with thickness of 300 μm have been subjected to high temperature testing in air in contact with V_2O_5 and CMAS. Two different reaction mechanisms were observed from the YSZ-V_2O_5 interaction depending on exposure temperature: formation of ZrV_2O_7 below 747 °C and formation of YVO_4 above 747 °C. Formation of YVO_4 resulted in the disruptive ZrO_2 phase transformation to monoclinic phase. Different degradation mechanisms were also observed for V_2O_5 melt interaction with CoNiCrAlY at 700 and 900 °C. At 700 °C, formation of (Cr, Al)VO_4 was dominant. However, at 900 °C, an extensive dissolution of CoNiCrAlY by V_2O_5 melt produced reaction products of $(Ni, Co)_3(VO_4)_2$ and (Ni, Co)$(Al, Cr)_2O_4$.

Molten CMAS was found to melt, readily infiltrate and degrade free-standing APS YSZ coatings at temperature above 1250 °C. CMAS melt readily dissolved the YSZ, and then reprecipitated ZrO_2 with a composition based on local melt chemistry that deviates in the content of the Y_2O_3 stabilizer. Extensive dissolution of the TGO α-Al_2O_3 from free-standing APS CoNiCrAlY coatings by CMAS melt was observed. A significant formation of spinel oxide was identified as degradation mechanisms.

Dense, crack-free, and uniform Al_2O_3 overlay coatings for TBCs were successfully fabricated by EPD followed by sintering at 1200 °C for 10 h. EPD Al_2O_3 overlay was found to protect the APS YSZ from CMAS attack. A change in CMAS composition to a crystallizable Al-rich composition promoted the formation of anorthite ($CaAl_2Si_2O_8$) platelets and $MgAl_2O_4$ spinel. Similarly, EPD MgO overlay was effective in protecting APS YSZ against V_2O_5 melt through thermochemical interactions that resulted in formation of magnesium vanadates that have higher melting temperature. Furnace thermal cyclic testing of TBCs on bond-coated superalloy, modified with 30 μm-thick EPD Al_2O_3 overlay demonstrated the promising durability.

Acknowledgments

This work was financially supported by the U.S. Department of Energy through University Turbine Systems Research program under the subcontract No. 02-01-SR118, State of Florida Turbine Initiative (SFTI) from National Aeronautics and Space Administration (NASA), and Florida Center for Advanced Aeronautics Propulsion (FCAAP). The authors are grateful to Dr. Bo Yao and Mr. Biao Yuan for their assistance in TEM characterization.

References

1. R.A. Miller, Oxidation-Based Model for Thermal Barrier Coating Life, *J. Am. Ceram. Soc.*, 1984, **67**(8), p 517-521
2. J. Stringer, Coatings in the Electricity Supply Industry: Past, Present, and Opportunities for the Future, *Surf. Coat. Technol.*, 1998, **108-109**, p 1-9
3. A.G. Evans, D.R. Mumm, J.W. Hutchinson, G.H. Meier, and F.S. Pettit, Mechanisms Controlling the Durability of Thermal Barrier Coatings, *Prog. Mater. Sci.*, 2001, **46**, p 505-553
4. N.P. Padture, M. Gell, and E.H. Jordan, Thermal Barrier Coatings for Gas-Turbine Engine Applications, *Science*, 2002, **296**, p 280-284
5. A.G. Evans, M.Y. He, and J.W. Hutchinson, Mechanism Based Scaling Laws for the Durability of Thermal Barrier Coatings, *Prog. Mater. Sci.*, 2001, **46**, p 249
6. A. Scrivani, U. Bardi, L. Carrafiello, A. Lavacchi, and F. Niccolai, A Comparative Study of High Velocity Oxygen Fuel, Vacuum Plasma Spray, and Axial Plasma Spray for the Deposition of CoNiCrAlY Bond Coat Alloy, *J. Therm. Spray Tech.*, 2003, **12**(4), p 504-507
7. R.L. Jones, Some Aspects of the Hot Corrosion of Thermal Barrier Coatings, *J. Therm. Spray Technol.*, 1997, **6**(1), p 77-84
8. P. Mohan, B. Yuan, T. Patterson, V.H. Desai, and Y.H. Sohn, Degradation of Yttria-Stabilized Zirconia Thermal Barrier Coatings by Vanadium Pentoxide, Phosphorous Pentoxide, and Sodium Sulfate, *J. Am. Ceram. Soc.*, 2007, **90**(11), p 3601-3607
9. C. Mercer, S. Faulhaber, A.G. Evans, and R. Darolia, A Delamination Mechanism for Thermal Barrier Coatings Subject to Calcium-Magnesium-Alumino-Silicate (CMAS) Infiltration, *Acta Mater.*, 2005, **53**(4), p 1029-1039
10. S. Kramer, J. Yang, and C.G. Levi, Thermochemical Interaction of Thermal Barrier Coatings with Molten CaO-MgO-SiO_2-Al_2O_3 (CMAS) Deposits, *J. Amer. Ceram. Soc.*, 2006, **89**(10), p 3167-3175
11. P. Mohan, B. Yuan, T. Patterson, V.H. Desai, and Y.H. Sohn, Degradation of Yttria-Stabilized Zirconia Thermal Barrier Coatings by Molten CMAS (CaO-MgO-Al_2O_3-SiO_2) Deposits, *Mater. Sci. Forum*, 2008, **595-598**, p 207-212
12. M.P. Borom, C.A. Johnson, and L.A. Peluso, Role of Environmental Deposits and Operating Surface Temperature in Spallation of Air Plasma Sprayed Thermal Barrier Coatings, *Surf. Coat. Technol.*, 1996, **86-87**, p 116-126
13. B.A. Nagaraj and D.J. Wortman, Burner Rig Evaluation of Ceramic Coatings with Vanadium-Contaminated Fuels, *Trans. ASME: J. Eng. Gas Turbines Power*, 1990, **112**, p 536-542
14. B.R. Marple, J. Voyer, C. Moreau, and D.R. Nagy, Corrosion of Thermal Barrier Coatings by Vanadium and Sulfur Compounds, *Mater. High Temp.*, 2000, **17**(3), p 397-412
15. R.L. Jones, C.E. Williams, and S.R. Jones, Reaction of Vanadium Compounds with Ceramic Oxides, *J. Electrochem. Soc.*, 1986, **133**(1), p 227-230
16. D.W. Sustitzky, W. Hertl, and C.B. Carter, Destabilization of Zirconia Thermal Barriers in the Presence of V_2O_5, *J. Am. Ceram. Soc.*, 1988, **71**(11), p 992-1004
17. P. Mohan, T. Patterson, V.H. Desai, and Y.H. Sohn, Degradation of Free-Standing Air Plasma Sprayed CoNiCrAlY Coatings by Vanadium and Phosphorus Pentoxides, *Surf. Coat. Technol.*, 2008, **203**, p 427-431
18. W.C. Hasz, M.P. Borom, and C.A. Johnson, Protection of Thermal Barrier Coating with an Impermeable Barrier Coating, U.S. Patent No. 5871820, 1999
19. W.C. Hasz, C.A. Johnson, and M.P. Borom, Protection of Thermal Barrier Coatings by a Sacrificial Surface Coating, U.S. Patent No. 5660885, 1997
20. P. Mohan, T. Patterson, and Y.H. Sohn, Electrophoretic Deposition of Environmental Barrier Overlay Coatings for Yttria-Stabilized Zirconia Thermal Barrier Coatings, *Proceedings of ASME Turbo Expo 2009: Power for Land, Sea and Air GT2009, GT2009-59839*
21. P. Mohan, B. Yao, T. Patterson, and Y.H. Sohn, Electrophoretically Deposited Alumina as Protective Overlay for Thermal Barrier Coatings Against CMAS Degradation, *Surf. Coat. Technol.*, 2009. doi:10.1016/j.surfcoat.2009.09.055
22. C. Batista, A. Portinha, R.M. Ribeiro, V. Teixeira, and C.R. Oliveira, Evaluation of Laser-Glazed Plasma-Sprayed Thermal Barrier Coatings Under High Temperature Exposure to Molten Salts, *Surf. Coat. Technol.*, 2006, **200**(24), p 6783-6791
23. A. Aygun, A.L. Vasiliev, N.P. Padture, and X. Ma, Novel Thermal Barrier Coatings that Are Resistant to High-Temperature Attack by Glassy Deposits, *Acta Mater.*, 2007, **55**, p 6734
24. R. Vassen, X. Cao, F. Tietz, D. Basu, and D. Stover, Zirconates as New Materials for Thermal Barrier Coatings, *J. Am. Ceram. Soc.*, 2000, **83**(8), p 2023-2028
25. S. Kramer, J. Yang, and C.G. Levi, Infiltration-Inhibiting Reaction of Gadolinium Zirconate Thermal Barrier Coatings with CMAS Melts, *J. Am. Ceram. Soc.*, 2008, **91**(2), p 576-583
26. L. Besra, C. Compson, and M. Liu, Electrophoretic Deposition on Non-Conducting Substrates: The Case of YSZ film on NiO-YSZ Composite Substrates for Solid Oxide Fuel Cell Application, *J. Power Sour.*, 2007, **173**, p 130-136
27. S.T. Aruna and K.S. Rajam, A Study on the Electrophoretic Deposition of 8YSZ Coating Using Mixture of Acetone and Ethanol Solvents, *Mater. Chem. Phys.*, 2008, **111**, p 131-136
28. O.O. Van der Biest and L.J. Vandeperre, Electrophoretic Deposition of Materials, *Annl. Rev. Mater. Sci.*, 1999, **29**, p 327-352
29. L. Besra and M. Liu, A Review on Fundamentals and Applications of Electrophoretic Deposition (EPD), *Prog. Mater. Sci.*, 2007, **52**, p 1-61